Nanoscale

PAPER

In situ loading of ultra-small Cu$_2$O particles on TiO$_2$ nanosheets to enhance the visible-light photoactivity†

Lichen Liu,[ab] Xianrui Gu,[ab] Chuanzhi Sun,[c] Hao Li,[ab] Yu Deng,*[b] Fei Gao*[b] and Lin Dong*[ab]

In this work, ultra-small Cu$_2$O nanoparticles have been loaded on TiO$_2$ nanosheets with {001} facets exposed through a one-pot hydrothermal reaction. These Cu$_2$O nanoparticles are well-dispersed on TiO$_2$ nanosheets with narrow size distributions and controllable sizes from 1.5 to 3.0 nm. Through XRD, TEM, N$_2$ absorption–desorption isotherms and UV-vis diffuse reflectance spectra, the Cu$_2$O/ TiO$_2$ nanosheets show similar phase structures, morphologies, pore structures as compared to pure TiO$_2$ nanosheets. Due to the loading of ultra-small Cu$_2$O nanoparticles, heterojunctions are formed between Cu$_2$O and TiO$_2$, which favors the efficient separation of photo-generated electrons and holes. Caused by the electron transfer from Cu$_2$O to TiO$_2$, Cu$_2$O/TiO$_2$ nanosheets show excellent visible-light activity, about 3 times that of N-doped TiO$_2$ nanosheets with {001} facets exposed. Furthermore, charge transfer rate across the interface of Cu$_2$O and TiO$_2$ shows great dependence on the size of Cu$_2$O particles. The charge transfer across the interface may be more efficient between TiO$_2$ nanosheets and smaller Cu$_2$O nanoparticles. Therefore, the Ti : Cu = 30 : 1(atomic ratio) sample shows the best activity due to its balance in light harvest and electron transfer rate in the degradation of phenol under visible light.

1. Introduction

TiO$_2$, as a wide-band-gap semiconductor, has drawn much attention because of its promising applications in utilization of solar energy derived from photocalysis, photovoltaics, and photocatalytic water splitting.[1–3] However the photocatalytic performance of traditional nanocrystalline TiO$_2$ is restricted by many factors, including the low absorption of solar light, fast recombination of photo-generated electrons and holes, and low photocatalytic activity on the conventional crystal facets. Thus, various strategies have been employed to prepare highly efficient TiO$_2$-based photocatalysts.[4–8]

Experimental results and theoretical calculations have demonstrated that surface modification of TiO$_2$ with metal oxide particles can be an efficient route to superior composite photo-catalytic materials.[9–11] The heterojunctions formed by TiO$_2$ and modified metal oxides contributes to the efficient separation of photo-generated electron–hole pairs, which minimizes the energy wasted caused by the electron–hole recombination.[12] Moreover, through loading metal oxide particles with narrow band gap on TiO$_2$, the obtained composites can show visible-light response because of the charge transfer across semiconductor interface. Metal oxides with narrow band gap (such as Cu$_2$O, Bi$_2$WO$_4$ and BiVO$_4$) were used as the sensitizers of TiO$_2$. Zhang *et al.* loaded polyhedral Cu$_2$O particles on TiO$_2$ nanotubes arrays through electrodeposition, and found significant improvement in the visible-light activity as compared to pure TiO$_2$ nanotubes.[13] Reported by Wang *et al.*, nanostructured Bi$_2$WO$_6$–TiO$_2$ prepared *via* an electrospinning technique also show much better photocatalytic activity under visible light because of the hetero-junctions between Bi$_2$WO$_6$ and TiO$_2$.[14]

However, in the previous reports, the size distributions of the modified particles on TiO$_2$ were usually hard to control. Usually, the metal oxide particles modified on TiO$_2$ are larger than 5 nm. As we know, the electronic structures of semiconductor nano-crystals show great dependence on the particle size,[15,16] therefore the sizes of the heterojunctions have direct influences on the photocatalytic activities. The charge transfer between TiO$_2$ and modified particles will greatly accelerate when the modified particles are as small as 2–3 nanometers due to the fast diffusion of charge carries.[17–19] In this regard, it is significant to prepare metal oxide nanoparticles loaded TiO$_2$ nanocomposites with homogeneous particle dispersion, ultrafine particle size, and narrow particle size distribution. Furthermore, little attention was paid to the crystal facets of TiO$_2$ in the metal oxide/TiO$_2$ composites previously. Mostly, in the conventional metal oxide/

[a]Key Laboratory of Mesoscopic Chemistry of Ministry of Education, School of Chemistry and Chemical Engineering, Nanjing University, Nanjing 210093, PR China

[b]Jiangsu Key Laboratory of Vehicle Emissions Control, Center of Modern Analysis, Nanjing University, Nanjing 210093, PR China. E-mail: dengyu@nju.edu.cn; gaofei@nju.edu.cn; donglin@nju.edu.cn; Fax: +86 25 83317761; Tel: +86 25 83592290

[c]Department of Chemistry, Chemical Engineering and Materials Science, Shandong Normal University, Jinan 250014, PR China

† Electronic supplementary information (ESI) available. See DOI: 10.1039/c2nr31859h

TiO$_2$ composites, the exposed crystal facets are {101} facets of anatase TiO$_2$. Recently, TiO$_2$ nanostructures with {001} facets exposed have attracted much attention due to the high activity of active {001} facets compared to conventional {101} facets.[20–22] Therefore, it will be feasible to build highly active TiO$_2$-based photocatalytic materials for visible-light applications through combining the advantages of metal oxide particles modification and active crystal facets.

In this work, for the first time, we successfully loaded ultra-small Cu$_2$O nanoparticles (*ca.* 2–3 nm) onto the surface of TiO$_2$ nanosheets with {001} facets exposed through a one-pot hydrothermal reaction. This method has the following advantages: (1) these Cu$_2$O particles are uniformly dispersed on TiO$_2$ nanosheets with narrow size distribution; (2) heterojunctions can form between TiO$_2$ and Cu$_2$O, which induces visible-light absorption and efficient separation of photo-generated electrons and holes. The Cu$_2$O/TiO$_2$ nanosheets (denoted as CT-NS for short) show much better photocatalytic activities under visible light as compared to N-doped TiO$_2$ nanosheets (N-TiO$_2$-NS) with {001} facets exposed (almost 3 times of N-TiO$_2$-NS), which can be ascribed to the p–n junctions between TiO$_2$ and Cu$_2$O. Herein, the structural features of Cu$_2$O/TiO$_2$ nanosheets and formation mechanisms are discussed, which may contribute to the synthesization of other metal (or metal oxide)/TiO$_2$ composite materials for energy and environmental applications.

2. Experimental

Synthesis of Cu$_2$O/TiO$_2$ nanosheets (CT-NS)

In the typical procedure for synthesis of CT-NS with the Ti : Cu ratio of 30 : 1, 0.5 g Cu(Ac)$_2$ was dissolved into 25 mL of Ti(OBu)$_4$ (TBOT) under stirring for 24 h, afterwards, a blue solution would be formed. Then 3 mL of hydrofluoric acid solution (40 wt%) were dropped to the above solution under strong stirring. After the addition of HF, the mixture was keep stirring for 1–2 h until it changed into gel. The gel was transferred into a dried Teflon autoclave with a capacity of 50 mL, and then kept at 180 °C for 24 h. After being cooled to room temperature, the white powder was separated by high-speed centrifugation and washed with ethanol and distilled water several times. At last, these products were dried in an electric oven under air flow at 110 °C for 8 h. In order to obtain F-free Cu$_2$O/TiO$_2$ nanosheets, 1.0 g power was dispersed in aqueous 0.1 M NaOH and stirred for 8 h at room temperature. The power was recovered by high-speed centrifugation and washed with distilled water and ethanol several times to neutral. Then, it was dried at 80 °C for 6 h.

Synthesis of pure TiO$_2$ nanosheets (TiO$_2$-NS)

Pure TiO$_2$ nanosheets were prepared by the hydrothermal method reported by Xie *et al.*,[23] which is similar to that of CT-NS. In a typical experimental procedure, 25 mL of Ti(OBu)$_4$ (TBOT) and 3 mL of hydrofluoric acid solution (40 wt%) were mixed in a dried Teflon autoclave with a capacity of 100 mL, and then kept at 180 °C for 24 h. After being cooled to room temperature, the white powder was separated by high-speed centrifugation and washed with ethanol and distilled water several times. At last, these products were dried in an electric oven under air flow at 80 °C for 6 h. The hydrothermal product

was also washed with aqueous 0.1 M NaOH to remove fluorine as described in the synthesis of Cu$_2$O/TiO$_2$ nanosheets.

Synthesis of N-doped TiO$_2$ nanosheets (N-TiO$_2$-NS)

N-doped TiO$_2$ nanosheets with {001} facets exposed were prepared according to the work by Yu.[24] In a typical synthesis, 0.2 g of TiN powder, 30 mL of absolute ethanol, 3 mL of 65 wt% nitric acid solution and 1.0 mL of 40 wt% hydrofluoric acid solution were mixed in a dried 50 mL Teflon-lined autoclave at room temperature, and then kept at 180 °C for 24 h. After cooling this autoclave to room temperature, a yellow precipitate was collected, washed with ethanol and distilled water three times, and then dried in an oven at 80 °C for 6 h.

Characterization

X-Ray diffraction (XRD) measurement patterns were recorded on a Philips X'pert Pro diffractometer using Ni-filtered Cu Kα1 radiation ($\lambda = 0.15$ nm). The X-ray tube was operated at 40 kV and 40 mA.

Transmission electron microscopy (TEM) images were taken on a JEM-2100 instrument at an acceleration voltage of 200 kV. The samples were crushed and dispersed in A.R. grade ethanol and the resulting suspensions were allowed to dry on carbon film supported on copper grids. Scanning transmission electron microscopy (STEM) images were taken on a high resolution transmission electron microscope (FEI TECNAI F30) with HAADF detector operator at 300 kV.

Field-emission scanning electron microscopy (FESEM) images were observed by a Hitachi S-4800 instrument at an acceleration voltage of 10 kV.

X-Ray fluorescence (XRF) spectroscopy analysis was operated on ARL ADVANT'X instrument, using Rh Kα radiation operating at 3600 W. The X-ray tube was operated at 60 kV and 120 mA.

X-Ray photoelectron spectroscopy (XPS) analysis was performed on a PHI 5000 VersaProbe system, using monochromatic Al Kα radiation (1486.6 eV) operating at 25 W. The sample was outgassed overnight at room temperature in a UHV chamber ($<5 \times 10^{-7}$ Pa). All binding energies (BE) were referenced to the C 1s peak at 284.6 eV. The experimental errors were within ±0.1 eV.

UV-vis diffuse reflectance spectroscopy (UV-vis DRS) was recorded in the range of 200–900 nm on a Shimadzu UV-2401 spectrophotometer with BaSO4 as reference.

Photoluminescence (PL) spectra were measured at room temperature on an F-7000 fluorescence spectrophotometer (Hitachi, Japan). The wavelength of the excitation light is 300 nm.

Measure of the photocatalytic activity

The photocatalytic activities of the CT-NS and TiO$_2$-NS for the degradation of phenol in an aqueous solution were measured under irradiation with a 300W Xe arc lamp equipped with an ultraviolet cutoff filter to provide visible light with $\lambda \geq 420$ nm. The sample (100 mg) was added to 40 mL phenol (10 mg L^{-1}) solution and stirred for 30 min without visible-light irradiation at room temperature in order to establish an adsorption–desorption equilibrium between phenol and the surface of the catalyst.

During the illumination, the suspension (3 mL) was collected at fixed intervals (1 h). The remaining solution was withdrawn for subsequent analysis with an UV-vis spectrophotometer (UV-3600 spectrometer).

3. Results and discussion

XRD was used to identify and determine the phase structures of Cu_2O/TiO_2 nanosheets (CT-NS) and pure TiO_2 nanosheets (TiO_2-NS). The XRD patterns of CT-NS and TiO_2-NS are displayed in Fig. 1. All samples show typical diffraction patterns of anatase TiO_2 (JCPDS no. 21-1272). No characteristic diffraction peaks responding to Cu or CuO_x appear, which implies a low loading content and poor crystallization of Cu species. Although the contents of Cu species are different in the CT-NS samples, their XRD patterns show similar shapes without obvious changes of intensities and widths. Moreover, no evident shift in the peak positions can be observed in each of the as-prepared CT-NS, indicating that no other ions have incorporated into the lattice of TiO_2. To further clarify the position of Cu species, Raman spectra were taken of TiO_2-NS and CT-NS. As presented in Fig. S1,† no differences between TiO_2-NS and CT-NS can be found. The positions of their E_g mode are almost the same, suggesting Cu ions do not dope into the frameworks of TiO_2 lattice. According to the XRD and Raman spectra results, we can deduce that some amorphous particles containing Cu species may form on the surface of TiO_2-NS in CT-NS samples.

Transmission electron microscopy (TEM) analysis was performed to characterize morphological differences between CT-NS and TiO_2-NS. Typical TEM images of CT(30 : 1) and pure TiO_2 nanosheets are displayed in Fig. 2. As show in Fig. 2a and c, both two samples consist of rectangular nanosheets with a side length of *ca.* 20–70 nm and thickness of *ca.* 4–8 nm. The HRTEM images in Fig. 2b and d show that the lattice spacing parallel to the top and bottom facets is ~0.235 nm, corresponding to the {001} planes of anatase TiO_2.[22] The TEM results indicate that TiO_2 nanosheets with {001} facets exposed are formed through hydrothermal treatment of HF and TBOT. Moreover, after comparing the morphologies of CT-NS and TiO_2-NS, we can
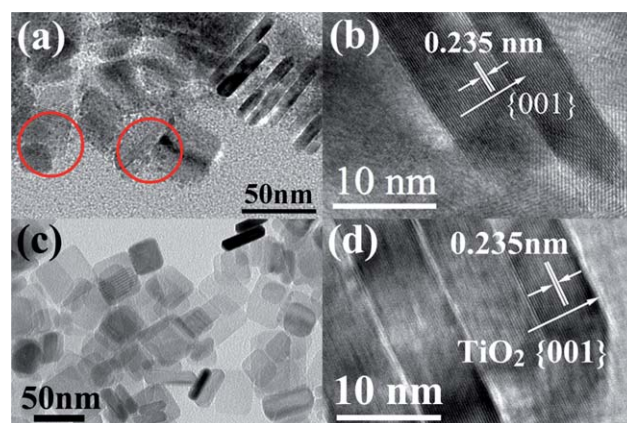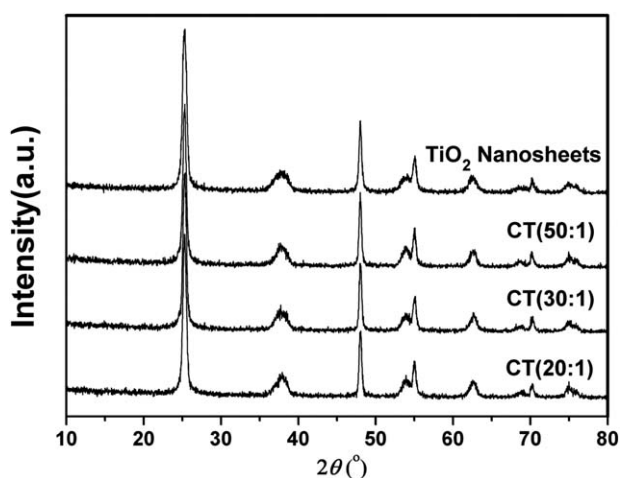

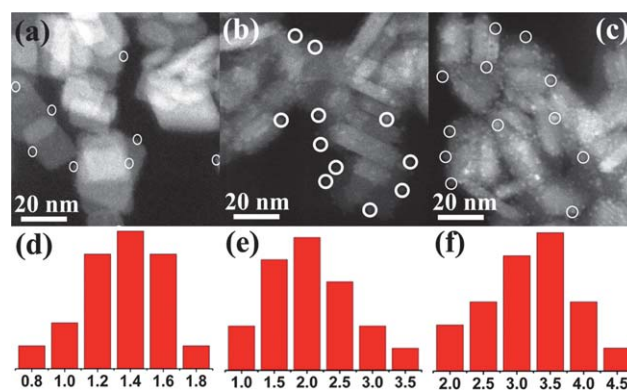**Fig. 2** (a and b) TEM images of Cu_2O/TiO_2 nanosheets, (c and d) TEM images of pure TiO_2 nanosheets.

find that the addition of copper species does not have an obvious influence on the morphologies of TiO_2 nanosheets. No other crystalline nanoparticles except for anatase TiO_2 can be found in CT-NS, which is in accordance with XRD results.

However, it's worthy to be noted that lots of ultra-small (~2 nm) particles can be seen on the surface of TiO_2 nanosheets in CT(30 : 1) (Fig. 2a), while the surface is quite smooth for TiO_2-NS (Fig. 2c). These small particles are well dispersed on the surface of TiO_2 nanosheets. Interestingly, they show amorphous structures without crystalline lattice fringes. Subsequently, scanning transmission electron microscopy (STEM) is employed to investigate these small particles in CT-NS. As shown in Fig. 3a–c, some ultra-small particles are dispersed on TiO_2 nanosheets in all CT-NS samples. The size distributions of the amorphous particles in each CT-NS are presented in Fig. 3d–f. The average size of the modified particles grows from 1.5 to 3.0 nm. According to the STEM images in Fig. 3, we can conclude that the size of the amorphous particles grows with the increase of Cu content, implying these ultra-small particles may be made up by compounds containing Cu element.

For further understanding on the amorphous particles, we have performed HRTEM studies. A single TiO_2 nanosheet is presented in Fig. 4a. Obviously, several amorphous particles are

Fig. 1 XRD patterns of pure TiO_2 nanosheets and Cu_2O/TiO_2 nanosheets.

Fig. 3 STEM images of Cu_2O/TiO_2 nanosheets and the size distributions of ultra-small nanoparticles supported on TiO_2 nanosheets: (a and d) CT(50 : 1); (b and e) CT(30 : 1); (c and f) CT(20 : 1).

located on the {001} facet of TiO$_2$ nanosheet, indicating that an interaction between the particle and TiO$_2$ support may exist. Subsequently, we carry out the following TEM experiments. A single amorphous particle is irradiated under the electron beam continually for several minutes, leading to transformation from an amorphous to a rystalline structure. As is presented in Fig. 4b and c, clear lattice fringes appear after the particle was irradiated for 2 min, which correspond to the (111) planes of metallic copper.[25] This HRTEM image reveals that the Cu nanocrystal appeared as a cubic close-packed (ccp) structure. This structural transformation may be due to the reduction of a compound containing Cu under the strong e-beam in TEM.[26] When the electronic irradiation was continued for another 1 min, the (111) lattice fringes transferred to fringes corresponding to (200) and (020) planes (Fig. 4d),[27] which suggests the formation of body-centered cubic (bcc) packing. This phase transformation is probably induced by the heating by e-beam. Although this kind of atomic rearrangement of metal nanocrystal has been reported for ruthenium,[28] platinum[29] and gold,[30,31] to our best of knowledge, it's the first time to observe the phase transformation of a copper nanocrystal under e-beam irradiation. Based on the above HRTEM results, we can conclude that amorphous nanoparticles containing a copper element can be *in situ* formed on TiO$_2$ nanosheets with active {001} faces exposed.

To address the chemical status of Cu element in the amorphous nanoparticle, X-ray photoelectron spectroscopy (XPS) analysis is carried out. The relative atomic ratios of various elements in Cu$_2$O/TiO$_2$ and pure TiO$_2$ nanosheets are listed in Table 1. X-Ray fluorescence (XRF) spectroscopy analysis is also performed for comparison as listed in Table 2. The amount of Cu element obtained from XPS is much larger than that obtained from XRF, which implies enrichment of Cu element may exist on the surface. This is understandable in view of the formation of nanoparticles containing Cu on TiO$_2$ nanosheets. The high-resolution XPS spectrum of Cu in the 2p region for CT(30 : 1) sample is displayed in Fig. 5. There are two peaks in Cu 2p$_{3/2}$ and Cu 2p$_{1/2}$ regions, respectively. According to previous reports, for the CuO$_x$ (Cu$_2$O, CuO or their mixture), Cu 2p$_{3/2}$ characteristic peaks for Cu$^+$ and Cu^{2+} appear around 932.6 (ref. 32) and
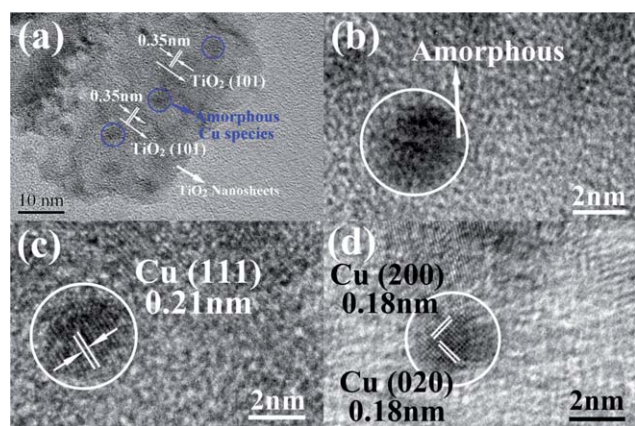
Table 1 Relative atomic ratios of various elements in pure TiO$_2$ nanosheets and Cu$_2$O/TiO$_2$ nanosheets measured by XPS

Sample	Ti (%)	O (%)	Cu (%)
TiO$_2$ nanosheets	30.12	69.87	—
CT (20 : 1)	29.35	68.70	1.95
CT (30 : 1)	29.40	69.10	1.50
CT (50 : 1)	29.57	69.08	1.35

933.7 eV (ref. 33). Thus, the peak located at 932.7 eV corresponds to Cu$^+$, which can be ascribed to Cu$_2$O on the surface of TiO$_2$ nanosheets.[34,35] Since Cu^{2+} can be reduced by solvent or reducing agent,[36] leading to formation of Cu$_2$O nanostructures, these amorphous particles may be Cu$_2$O formed from the hydrolysis and reduction of Cu(Ac)$_2$ in the hydrothermal process. Furthermore, no peaks corresponding to Cu^{2+} in CuO can be found neighboring 933.6 eV, indicating that Cu species mainly exist as Cu$_2$O. Notably, a small peak located at 934.9 eV can be found, which may originate from Cu^{2+} in Cu(Ac)$_2$.[37] Cu(Ac)$_2$ was used as precursor in the hydrothermal process, which may remain on the surface of TiO$_2$ nanosheets. Aiming to confirm the identification of this peak, XPS spectra of Cu(Ac)$_2$ were tested (see Fig. 5b) and the results show that the 934.7 eV peak can be ascribed to Cu^{2+} in Cu(Ac)$_2$. Based on the TEM and XPS characterizations, we can conclude that small Cu$_2$O nanoparticles have formed on the surface of TiO$_2$ nanosheets. Although Cu^{2+} can be detected on the surface of CT-NS, the amount is much smaller as compared to Cu$^+$. Thus, the Cu species in CT-NS should mainly exist as Cu$_2$O.

In order to investigate the chemical stability of Cu$_2$O during photocatalysis, we test its XPS spectrum of CT(30 : 1) after six photocatalytic cycles. From Fig. 5c we can figure out that the 2p$_{3/2}$ peak of Cu 2p region locates at 932.5 eV, which can be ascribed to Cu$_2$O, indicating the stability of Cu$_2$O nanoparticles during the photocatalysis reaction. Notably, the small peak corresponding to Cu(Ac)$_2$ disappears in the used sample. This change of the Cu species should be caused by the interface charge transfer from TiO$_2$ to Cu(Ac)$_2$. Under visible-light irradiation, the electron can transfer from the valence band to the surface Cu(Ac)$_2$ through interface charge transfer, leading to the reduction of Cu^{2+} to Cu$^+$.[38] In the CT(30 : 1) sample, the Cu(Ac)$_2$ absorbed on the TiO$_2$ nanosheets in the fresh sample can be reduced to Cu$_2$O under irradiation. As a result, the peak corresponding to Cu(Ac)$_2$ disappears in the used sample. Based on the XPS analysis, we can find that ultra-small Cu$_2$O nanoparticles are stable enough during the photocatalytic process.

The effects of Cu$_2$O loading on the pore structure and BET surface areas of as-prepared CT-NS samples are investigated by

Fig. 4 (a) TEM image of a single TiO$_2$ nanosheet in CT(30 : 1). (b and c) HRTEM images of an amorphous particle under e-beam. The phase transformation of this nanoparticle can be seen: from amorphous to crystalline.

Table 2 The relative atomic ratios of various elements in pure TiO$_2$ nanosheets and Cu$_2$O/TiO$_2$ nanosheets measured by XRF

Sample	Ti (%)	O (%)	Cu (%)
TiO$_2$ nanosheets	33.33	66.67	—
CT (20 : 1)	32.82	66.41	0.77
CT (30 : 1)	32.97	66.49	0.54
CT (50 : 1)	33.03	66.62	0.35
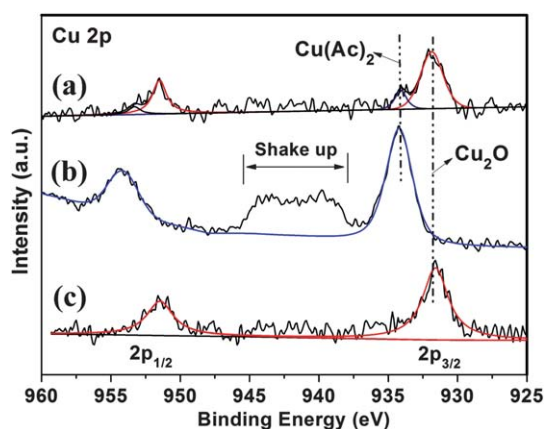
Fig. 5 High-resolution XPS spectra of Cu 2p region for fresh CT(30 : 1) (a), $Cu(Ac)_2$ (b) and used CT(30 : 1) after six cycles.

the N_2 adsorption–desorption measurement. It can be seen from Fig. 6a that TiO_2-NS and CT-NS have isotherms of type IV from the Brunauer–Deming–Deming–Teller (BDDT) classification, indicating the presence of mesopores (2–50 nm).[39] The corresponding hysteresis loops are type H3 at a high relative pressure
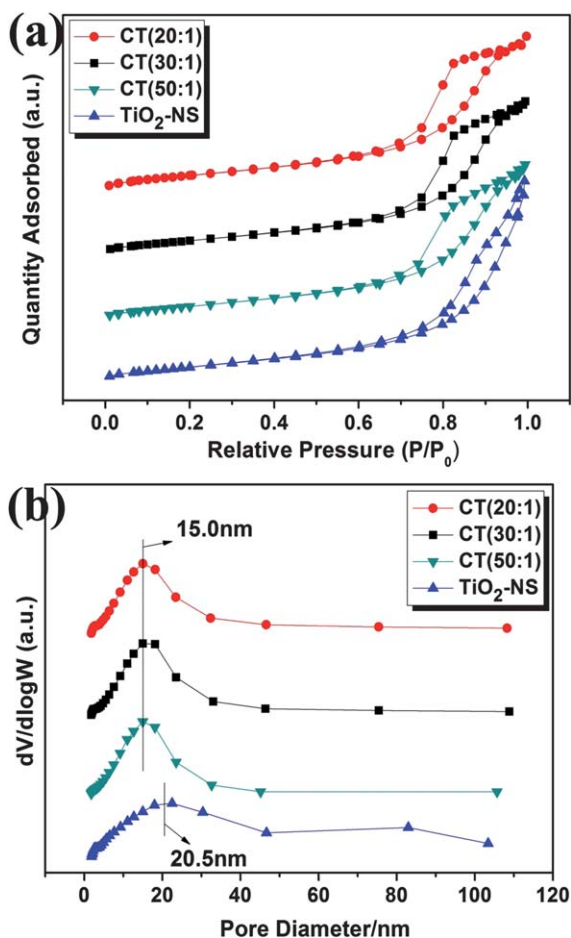
Fig. 6 (a) N_2 absorption–desorption isotherms of pure TiO_2 nanosheets and Cu_2O/TiO_2 nanosheets. (b) Pore size distributions of pure TiO_2 nanosheets and Cu_2O/TiO_2 nanosheets.

range of 0.75 to 1.0, suggesting the presence of slit-like pores. Since the TiO_2-NS and CT-NS do not contain intrinsic mesopores and macropores, the generation of hysteresis loops is from the aggregation of the sheet-like TiO_2 nanoparticles.[40] If we compare these hysteresis loops carefully, we can find that the CT-NS samples show relatively narrow hysteresis loops located at 0.8 to 0.9. This difference can also be reflected in the pore size distributions of TiO_2-NS and CT-NS (Fig. 6b). Obviously, in CT-NS, all of them show narrow size distributions with an average pore size of 15.0 nm. As for pure TiO_2 nanosheets, they show a wider size distribution as compared to CT-NS samples and a larger average pore size of 20.5 nm. The BET surface area and pore volume for these samples are listed in Table 3. Although there are small differences between TiO_2-NS and CT-NS in pore volume and surface areas, the influences induced by addition of Cu_2O nanoparticles are limited. The CT-NS show a slightly decrease in specific surface areas and pore volumes, which can be ascribed to the decrease of cracks between TiO_2 nanosheets caused by loading of Cu_2O nanoparticles. Therefore, we can consider that the pore structures of TiO_2-NS and CT-NS are almost the same, which is in agreement with their similar morphologies.

Fig. 7 shows UV-vis diffuse reflectance spectra and digital photos of the Cu_2O/TiO_2 and pure TiO_2 nanosheets. TiO_2-NS show typical UV-vis diffuse reflectance spectra of anatase with a cut-off wavelength at $\sim$400 nm, corresponding to its band gap of 3.2 eV.[1,3] As for CT-NS, a broad visible-light absorption at 400–1000 nm can be seen in all CT-NS, indicating their promising applications for utilization of solar energy. An absorption shoulder corresponding to interface charge transfer (IFCT) from TiO_2 VB to Cu_2O can be found at $\sim$450 nm.[10,11] Since Cu_2O is a semiconductor with a narrow band gap ($\sim$2.0 eV) as compared to anatase TiO_2, Cu_2O can be excited by visible light, leading to absorption at 500–700 nm.[13,41] Caused by this visible-light response, CT(30 : 1) show pink color in the digital photo. Specially, the CT-NS show absorption in the 750–1000 nm region, and the intensity increases with the content of copper. This absorption region can be assigned to the d–d transition of Cu(II) in $Cu(Ac)_2$ absorbed on TiO_2 nanosheets as confirmed by XPS.[38] For CT-NS, their cutoff wavelength are all located at $\sim$400 nm. Notably, no blue- or red shift can be observed in the cutoff wavelength of CT-NS compared to TiO_2-NS, suggesting that the addition of Cu_2O does not change the band gap of TiO_2 nanosheets, except for introduction of visible-light absorption.

In previous reports, the heterojunctions were usually built to favor the separation of photo-generated electrons and holes.[9,42] The UV-vis diffuse reflectance spectra have already confirmed the formation of Cu_2O–TiO_2 heterojunction. To address the

Table 3 The BET surface area, pore volume and average pore sizes of TiO_2 nanosheets and Cu_2O/TiO_2 nanosheets

Sample	S_{BET} (m^2 g^{-1})	Pore volume (cm^3 g^{-1})	Average pore size (nm)
TiO_2 nanosheets	103.7	0.30	20.5
CT (20 : 1)	98.9	0.28	15.0
CT (30 : 1)	93.7	0.27	15.0
CT (50 : 1)	97.9	0.28	15.0
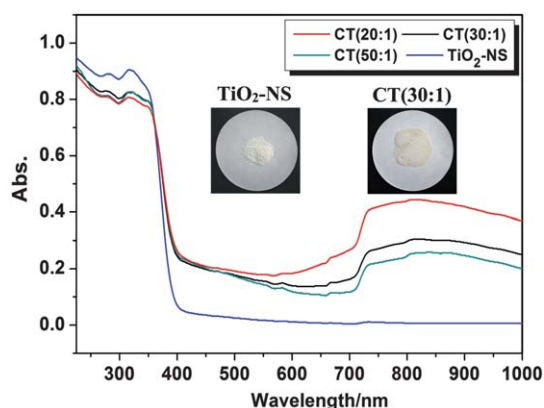
Fig. 7 UV-vis diffuse reflectance spectra of pure TiO_2 sheets and Cu_2O/TiO_2 nanosheets. Digital photos of pure TiO_2 nanosheets and CT(30 : 1) are also presented.

effect of Cu_2O–TiO_2 heterojunction on electron–hole separation, we employ photoluminescence spectra (PL spectra) to characterize the recombination probability in pure TiO_2 nanosheets and Cu_2O/TiO_2 nanosheets. PL spectra in the wavelength of 350–575 nm of TiO_2-NS and CT-NS are displayed in Fig. 8. No obvious emission peak can be found around 400 nm, suggesting that these PL signals do not result directly from the electron transition from the conduction band to valence band.[43–45] All of these samples show similar curves with four emission peaks located at 450, 468, 482 and 492 nm. The PL peaks at 450 and 468 nm are corresponding to band edge free excitons.[44] In addition, peaks at 482 and 492 nm are attributed to excitonic PL signals, which are related to surface oxygen vacancies or defects in TiO_2-NS or CT-NS.[43] The PL intensities of CT-NS are lower than that of TiO_2 nanosheets, implying lower electron–hole recombination probability in CT-NS. Combining UV-vis diffuse reflectance spectra, the PL spectra have further confirmed the formation of heterojunctions between Cu_2O and TiO_2. When TiO_2 and Cu_2O are excited by the excitation light, electrons and holes are formed. Because of the electric field in Cu_2O–TiO_2, electrons and holes are separated by the p–n junctions,[41] leading to a decrease of PL intensity in CT-NS. The CT(30 : 1) sample shows the lowest PL intensity, implying its high efficiency in electron–hole separation.
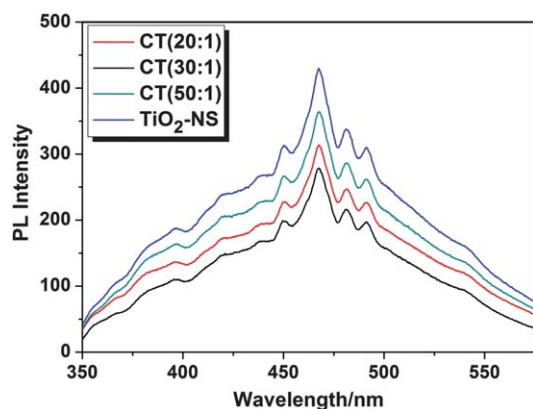

Fig. 8 PL spectra of pure TiO_2 nanosheets and Cu_2O/TiO_2 nanosheets.

To shed light on the formation mechanism of Cu_2O/TiO_2 nanosheets, their growth process was followed by examining the products harvested at different intervals of reaction time. The precipitates obtained at different reaction times were characterized by electron TEM (Fig. 9). As shown in Fig. 9a, only small TiO_2 nanoparticles (5–20 nm) were formed after 6 h. These particles showed irregular shapes and no Cu_2O nanoparticles could be found on TiO_2. When the reaction time was increased to 12 h, TiO_2 nanoparticles became larger and a few Cu_2O nanoparticles appeared (Fig. 9b). Further prolonging the reaction time would lead to the formation of rectangular TiO_2 nanosheets with Cu_2O nanoparticles located on the surface (Fig. 9c). The XRD patterns of these products (Fig. 10) further revealed that crystallization could be improved with the increase of reaction time. Based on the above results, the formation mechanism of CT-NS is described in Fig. 9d. Poor crystalline TiO_2 nanoparticles are first formed through the hydrolysis of TBOT at the initial stage of the hydrothermal reaction. With prolongation of the reaction time, crystallization improved and Cu_2O nanoparticles appear on the surface of TiO_2 nanosheets due to the hydrolysis and reduction of $Cu(Ac)_2$. Although Cu_2O/TiO_2 composites have been prepared through other methods,[46–49] the size and particle dispersion of Cu_2O is hard to control. In our work, ultra-small Cu_2O nanoparticles can be loaded onto TiO_2 nanosheets with controllable sizes as a result of slow hydrolysis and reduction of $Cu(Ac)_2$.

The photocatalytic activity of the as-prepared pure TiO_2 nanosheets and Cu_2O/TiO_2 nanosheets is evaluated by photodegradation of phenol under visible-light irradiation. According to previous reports, N-doped TiO_2 nanosheets (N-TiO_2-NS) with {001} facets exposed is a superior photocatalyst under visible light.[24] Thus, we have prepared N-doped TiO_2 nanosheets for comparison to evaluate the catalytic performance of CT-NS. The structure and morphology characterizations can be seen in Fig. S2.† The degradation curves are displayed in Fig. 11. TiO_2-NS show very poor activity due to their weak absorption of visible light. N-TiO_2-NS show enhanced photoactivity, which can be attributed to N-doping according to UV-vis diffuse reflectance spectra. As for CT-NS, the three samples with different Cu content show better degradation efficiency as compared to TiO_2-NS and N-TiO_2-NS. Especially, CT(30 : 1) exhibits the best performance, almost 3 times that of N-TiO_2-NS calculated from the kinetic constants (Fig. 11b). The stability of CT(30 : 1) has also been tested as shown in Fig. 12. This sample still shows quite an excellent catalytic performance after six cycles.

Based on the TEM results, no obvious morphological differences can be observed between Cu_2O/TiO_2 nanosheets and pure TiO_2 nanosheets. Furthermore, The XRD patterns, N_2 absorption–desorption isotherms and UV-vis diffuse reflectance spectra have demonstrated that the phase structures, porous structures and band structures show limited differences between pure TiO_2-NS and CT-NS. Thus, the enhanced photocatalytic efficiency for CT-NS should be attributed to the heterojunctions between TiO_2 and Cu_2O. As we know, anatase TiO_2 is an n-type semiconductor (band gap $\approx$ 3.2 eV),[3] while Cu_2O is a p-type semiconductor (band gap $\approx$ 2.0 eV),[50,51] which overlaps with that of anatase. Thus, When Cu_2O nanoparticles are loaded onto the surface of TiO_2 nanosheets, p–n heterojunctions will form.[41,52] The energy
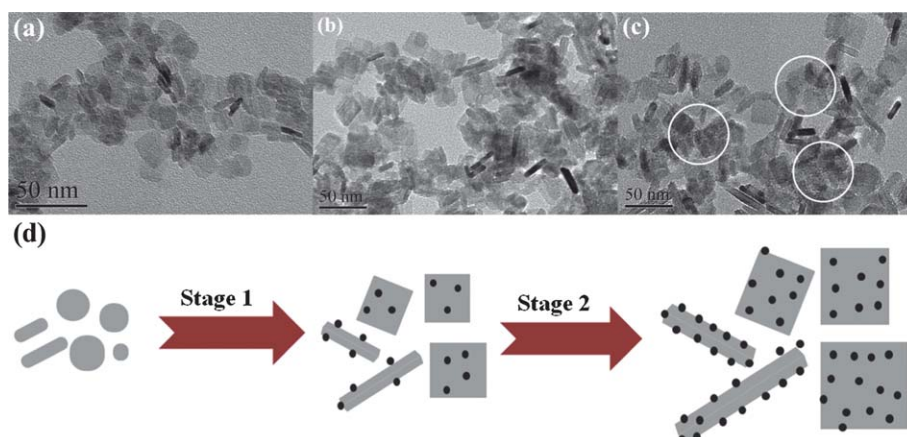
Fig. 9 TEM images of products obtained at different time during the hydrothermal reaction for preparation of CT(30 : 1): (a) 6 h; (b) 12 h; (c) 18 h. (d) Schematic illustration of the formation mechanism of Cu_2O/TiO_2 nanosheets.
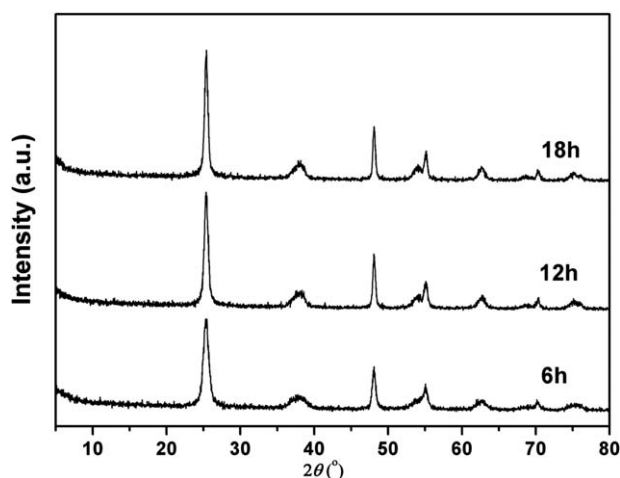
Fig. 10 XRD patterns of products obtained at different times during the hydrothermal reaction.

band diagram of $Cu_2O–TiO_2$ heterojunction is presented in Fig. 13a. Since the photocatalytic test is carried out under visible light, only Cu_2O will be excited due to its narrow band gap. According to the band structure, electrons excited by the visible light in p-Cu_2O will move to the n-TiO_2 side. The charge transfer across the heterojunction interface has been confirmed by the decrease of PL intensities for CT-NS. Caused by this charge flow, the efficiency of the use of visible light can be significantly improved, leading to higher photoactivity. Previous works have demonstrated that TiO_2 nanostructures with {001} facets exposed show superior photocatalytic performance due to the high activity of {001} facets.[20–23] In our work, when electrons transfer to TiO_2 nanosheets from Cu_2O nanoparticles, active radicals (e.g. O_2^-) will form, which leads to the degradation of phenol. These CT-NS have combined the advantages of heterojunctions and active crystal facets, as a result of which they show excellent visible-light activity.

According to the previous experimental and theoretical works, the electron transfer rates in semiconductor junctions show great dependence on the particle size. Based on the Marcus theory, electron transfer across the semiconductor interface will greatly
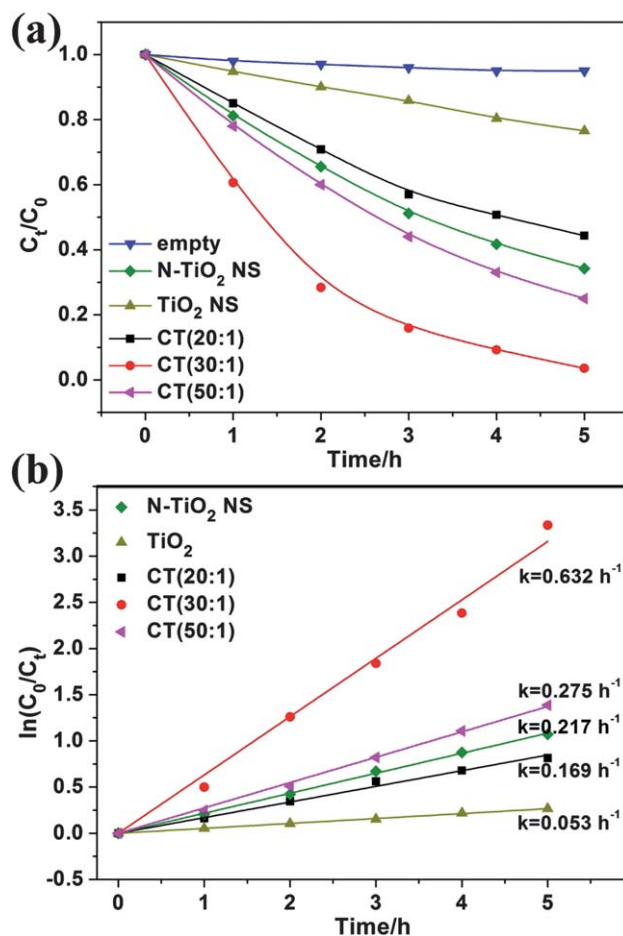
Fig. 11 (a) Degradation curves and (b) kinetic curves of phenol catalyzed by pure TiO_2 nanosheets and Cu_2O/TiO_2 nanosheets under visible light.

accelerate when the particle size of the electron donor decreases to 2–3 nm.[17,53] In our work, as shown in Fig. 3, CT-NS with different Cu_2O particle sizes (1.5, 2.0 and 3.0 nm) have been prepared. The electron transfer will increase with the decrease of Cu_2O particle size in accordance with the Marcus theory. From
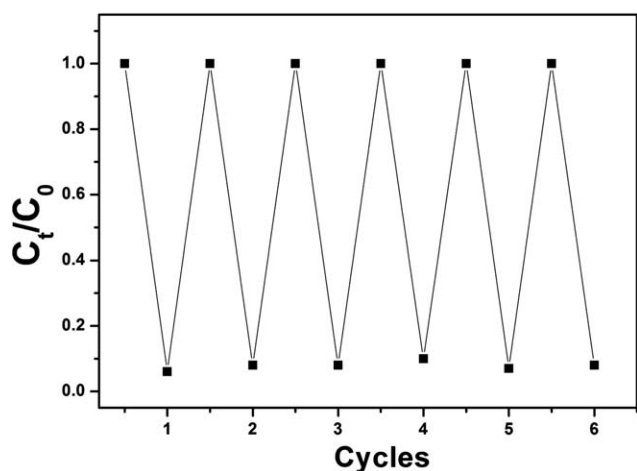
Fig. 12 Photocatalytic stability of CT(30 : 1) for six cycles.

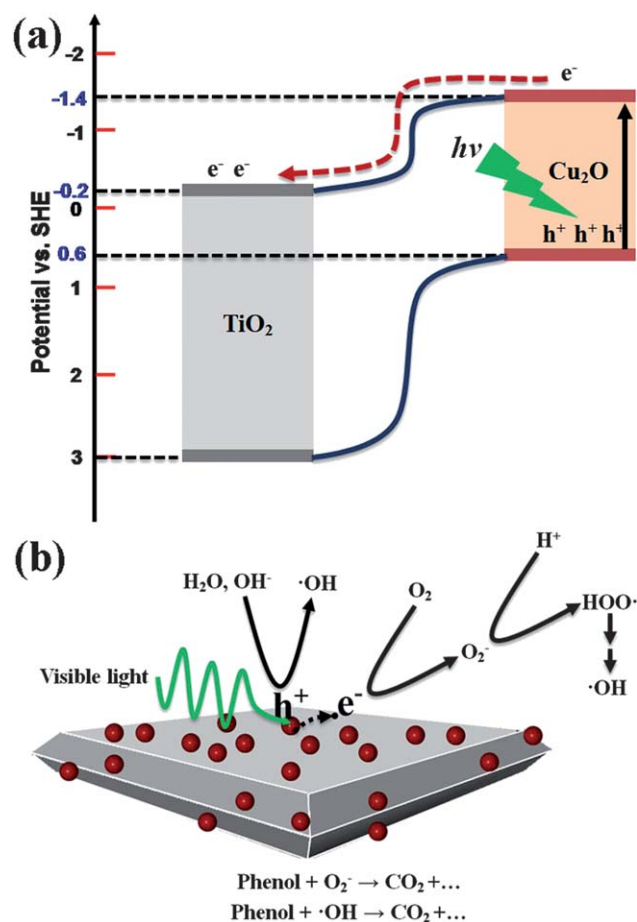**Fig. 13** (a) Energy diagram of Cu_2O–TiO_2 heterojunction and the electron flow from p-Cu_2O to n-TiO_2 under visible light excitation. (b) Mechanism of the photocatalytic degradation of phenol by Cu_2O/TiO_2 nanosheets under visible light.

Fig. 10, we can figure out that the photocatalytic activities of CT-NS follow this order: CT(30 : 1) > CT(50 : 1) > CT(20 : 1). Although CT(50 : 1) has the highest charge transfer constant, the low content of Cu_2O restricts its absorption of visible light. As

for CT(30 : 1), more Cu_2O nanoparticles are loaded on TiO_2 nanosheets for visible light harvest. More importantly, electron transfer from Cu_2O to TiO_2 still keeps fast enough in 2 nm-large Cu_2O particles. In CT(20 : 1), the electron transfer rate may decline when Cu_2O nanoparticles are as large as 3.0 nm, leading to photo-generated electron–hole recombination in Cu_2O and relatively poor photocatalytic activity.

In the light of the above characterizations and analysis, a possible catalytic mechanism for CT-NS is shown in Fig. 13b. When CT-NS were irradiated by visible light, the electrons in Cu_2O VB were excited to Cu_2O CB. Subsequently, the photo-generated electrons can transfer to TiO_2 CB, resulting the separation of holes and electrons. Then, active radicals ($\cdot OH$, O_2^-) were generated by the electrons and holes, which initiated the degradation of phenol.[54,55] Since CT(30 : 1) combines the balance of light harvest and efficient electron transfer, it shows the best visible-light photoactivity as compared to CT(50 : 1) and CT (20 : 1).

4. Conclusions

In conclusion, ultra-small Cu_2O nanoparticles have been loaded on TiO_2 nanosheets through a one-pot hydrothermal reaction. These Cu_2O nanoparticles are well-dispersed on TiO_2 nanosheets with narrow size distributions and controllable sizes from 1.5 to 3.0 nm. It is proven that the loading of Cu_2O nanoparticles does not show obvious influence on the morphologies, phase structures, pore structures and band structures of TiO_2 nanosheets. Therefore, it should be the Cu_2O–TiO_2 heterojunction that enhances the visible-light activity of CT-NS. Due to the loading of ultra-small Cu_2O nanoparticles, heterojunctions are formed between Cu_2O and TiO_2, which favors the efficient separation of photo-generated electrons and holes. Caused by the electron transfer from Cu_2O to TiO_2, Cu_2O/TiO_2 nanosheets show much better visible-light photocatalytic performance than pure TiO_2 nanosheets. By combining the advantages of heterojunctions and active anatase {001} facets, CT-NS show much better visible-light activity than N-doped TiO_2 nanosheets with {001} facets exposed. Furthermore, charge transfer rate across the interface of Cu_2O and TiO_2 shows great dependence on the size of Cu_2O particles. Therefore, CT(30 : 1) sample shows the best activity due to its balance in light harvest and electron transfer rate in the degradation of phenol under visible light. Our work may contribute to the synthesis of a new metal oxide (or metal)/TiO_2 for energy and environmental applications.

Acknowledgements

References

1 X. Chen and S. S. Mao, *Chem. Rev.*, 2007, **107**, 2891–2959.
2 X. B. Chen, S. H. Shen, L. J. Guo and S. S. Mao, *Chem. Rev.*, 2010, **110**, 6503.
3 A. Fujishima, X. Zhang and A. D. Tryk, *Surf. Sci. Rep.*, 2008, **63**, 515.
4 R. Asahi, T. Morikawa, T. Ohwaki, K. Aoki and Y. Taga, *Science*, 2001, **293**, 269–271.

5 X. Chen, L. Liu, P. Y. Yu and S. S. Mao, *Science*, 2011, **331**, 746–750.
6 M. Kong, Y. Li, X. Chen, T. Tian, P. Fang, F. Zheng and X. Zhao, *J. Am. Chem. Soc.*, 2011, **133**, 16414–16417.
7 H. G. Yang, C. H. Sun, S. Z. Qiao, J. Zou, G. Liu, S. C. Smith, H. M. Cheng and G. Q. Lu, *Nature*, 2008, **453**, 638–641.
8 Y. Tian and T. Tatsuma, *J. Am. Chem. Soc.*, 2005, **127**, 7632–7637.
9 M. Nolan, *Chem. Commun.*, 2011, **47**, 8617.
10 H. Tada, Q. Jin, H. Nishijima, H. Yamamoto, M. Fujishima, S.-i. Okuoka, T. Hattori, Y. Sumida and H. Kobayashi, *Angew. Chem., Int. Ed.*, 2011, **50**, 3501–3505.
11 H. Yu, H. Irie, Y. Shimodaira, Y. Hosogi, Y. Kuroda, M. Miyauchi and K. Hashimoto, *J. Phys. Chem. C*, 2010, **114**, 16481–16487.
12 J. S. Jang, H. G. Kim and J. S. Lee, *Catal. Today*, 2012, **185**, 270–277.
13 S. Zhang, S. Zhang, F. Peng, H. Zhang, H. Liu and H. Zhao, *Electrochem. Commun.*, 2011, **13**, 861–864.
14 Y. Zhang, L. Fei, X. Jiang, C. Pan, Y. Wang and A. Srivastava, *J. Am. Ceram. Soc.*, 2011, **94**, 4157–4161.
15 R. Rossetti, J. L. Ellison, J. M. Gibson and L. E. Brus, *J. Chem. Phys.*, 1984, **80**, 4464–4469.
16 L. E. Brus, *J. Chem. Phys.*, 1984, **80**, 4403–4409.
17 P. V. Kamat, *J. Phys. Chem. Lett.*, 2012, **3**, 663–672.
18 W. A. Tisdale, K. J. Williams, B. A. Timp, D. J. Norris, E. S. Aydil and X. Y. Zhu, *Science*, 2010, **328**, 1543–1547.
19 K. Tvrdy, P. Frantszov and P. V. Kamat, *Proc. Natl. Acad. Sci. U. S. A.*, 2011, **108**, 29–34.
20 G. Liu, J. C. Yu, G. Q. Lu and H. M. Cheng, *Chem. Commun.*, 2011, **47**, 6763.
21 C. Z. Wen, H. B. Jiang, S. Z. Qiao, H. G. Yang and G. Q. Lu, *J. Mater. Chem.*, 2011, **21**, 7052.
22 G. Liu, L. Wang, H. G. Yang, H. M. Cheng and G. Q. Lu, *J. Mater. Chem.*, 2010, **20**, 831.
23 X. G. Han, Q. Kuang, M. S. Jin, Z. X. Xie and L. S. Zheng, *J. Am. Chem. Soc.*, 2009, **131**, 3152.
24 Q. Xiang, J. Yu, W. Wang and M. Jaroniec, *Chem. Commun.*, 2011, **47**, 6906–6908.
25 M. Cao, C. Hu, Y. Wang, Y. Guo, C. Guo and E. Wang, *Chem. Commun.*, 2003, 1884–1885.
26 M. Y. Yen, C. W. Chiu, F. R. Chen, J. J. Kai, C. Y. Lee and H. T. Chiu, *Langmuir*, 2004, **20**, 279.
27 P. L. Hansen, J. B. Wagner, S. Helveg, J. R. Rostrup-Nielsen, B. S. Clausen and H. Topsoe, *Science*, 2002, **295**, 2053.
28 J.-O. Malm, J.-O. Bovin, A. Petford-Long, D. J. Smith, G. Schmid and N. Klein, *Angew. Chem., Int. Ed. Engl.*, 1988, **27**, 555–558.
29 L. R. Wallenberg and J.-O. Bovin, *Ultramicroscopy*, 1986, **20**, 71–76.
30 D. J. Smith, A. K. Petford-Long, L. R. Wallenberg and J.-O. Bovin, *Science*, 1986, **233**, 872–875.
31 X. Huang, S. Li, Y. Huang, S. Wu, X. Zhou, S. Li, C. L. Gan, F. Boey, C. A. Mirkin and H. Zhang, *Nat. Commun.*, 2011, **2**, 292.
32 J. P. Espinos, J. Morales, A. Barranco, A. Caballero, J. P. Holgado and A. R. Gonzalez-Elipe, *J. Phys. Chem. B*, 2002, **106**, 6921–6929.
33 C. Sun, J. Zhu, Y. Lv, L. Qi, B. Liu, F. Gao, K. Sun, L. Dong and Y. Chen, *Appl. Catal., B*, 2011, **103**, 206–220.
34 L. Huang, F. Peng and F. S. Ohuchi, *Surf. Sci.*, 2009, **603**, 2825–2834.
35 L. Gou and C. J. Murphy, *Nano Lett.*, 2003, **3**, 231–234.
36 C.-H. Kuo and M. H. Huang, *Nano Today*, 2010, **5**, 106–116.
37 J. F. Moulder, W. F. Stickle, P. E. Sobol and K. D. Bomben, *Handbook of X-ray Photoelectron Spectroscopy*, Perkin-Elmer Corp., USA, 1992.
38 J. Yu and J. Ran, *Energy Environ. Sci.*, 2011, **4**, 1364–1371.
39 C. Sun, L. Liu, L. Qi, H. Li, H. Zhang, C. Li, F. Gao and L. Dong, *J. Colloid Interface Sci.*, 2011, **364**, 288–297.
40 K. Lv, Q. Xiang and J. Yu, *Appl. Catal., B*, 2011, **104**, 275–281.
41 S. Chu, X. Zheng, F. Kong, G. Wu, L. Luo, Y. Guo, H. Liu, Y. Wang, H. Yu and Z. Zou, *Mater. Chem. Phys.*, 2011, **129**, 1184–1188.
42 F. Lin, D. Wang, Z. Jiang, Y. Ma, J. Li, R. Li and C. Li, *Energy Environ. Sci.*, 2012, **5**, 6400–6406.
43 L. Jing, H. Fu, B. Wang, D. Wang, B. Xin, S. Li and J. Sun, *Appl. Catal., B*, 2006, **62**, 282–291.
44 B. Liu, X. Wang, G. Cai, L. Wen, Y. Song and X. Zhao, *J. Hazard. Mater.*, 2009, **169**, 1112–1118.
45 X. Z. Li, F. B. Li, C. L. Yang and W. K. Ge, *J. Photochem. Photobiol., A*, 2001, **141**, 209–217.
46 Y. G. Zhang, L. L. Ma, J. L. Li and Y. Yu, *Environ. Sci. Technol.*, 2007, **41**, 6264–6269.
47 Y. Hou, X. Y. Li, X. J. Zou, X. Quan and G. H. Chen, *Environ. Sci. Technol.*, 2009, **43**, 858–863.
48 L. Yang, S. L. Luo, Y. Li, Y. Xiao, Q. Kang and Q. Y. Cai, *Environ. Sci. Technol.*, 2010, **44**, 7641–7646.
49 K. Lalitha, G. Sadanandam, V. D. Kumari, M. Subrahmanyam, B. Sreedhar and N. Y. Hebalkar, *J. Phys. Chem. C*, 2010, **114**, 22181–22189.
50 J. Ghijsen, L. H. Tjeng, J. van Elp, H. Eskes, J. Westerink and G. A. Sawatzky, *Phys. Rev. B*, 1988, **38**, 11322.
51 L. I. Hung, C. K. Tsung, W. Y. Huang and P. D. Yang, *Adv. Mater.*, 2010, **22**, 1910–1914.
52 L. Huang, F. Peng and F. S. Ohuchi, *Surf. Sci.*, 2009, **603**, 2825–2834.
53 Y. Q. Cao, Y. Georgievskii and R. A. Marcus, *J. Chem. Phys.*, 2000, **112**, 3358–3369.
54 S. Liu, C. Liu, W. Wang, B. Cheng and J. Yu, *Nanoscale*, 2012, **4**, 3193–3200.
55 W. Li, D. Li, Y. Li, P. Wang, W. Chen, X. Fu and Y. Shao, *J. Phys. Chem. C*, 2012, **116**, 3552–3560.